Thermomechanical Analysis of the Cyclic Behavior of Materials

André Chrysochoos

Available online at www.sciencedirect.com

SciVerse ScienceDirect

Procedia IUTAM 4 (2012) 15 – 26

Procedia IUTAM

www.elsevier.com/locate/procedia

Full field measurements and identification in Solid Mechanics

Thermomechanical Analysis of the Cyclic Behavior of Materials

André Chrysochoos

Mechanics and Civil Engineering Laboratory, Montpellier University, CC 048, Place E. Bataillon, 34095 Montpellier Cedex 05, France

Abstract

The cyclic behavior of materials often shows stabilized hysteretic responses. The present paper aims at highlighting the advantages of combining digital image correlation (DIC) and infrared thermography (IRT) to identify the energy nature of such hysteresis loops. Dissipative mechanisms are generally responsible for the mechanical energy lost in the stress-strain loop, reflecting irreversible material degradation. Thermodynamic analysis of the cyclic responses however revealed that such hysteresis areas may not only be induced by intrinsic dissipation but also by internal energy variations (stored energy) and/or by strong thermomechanical coupling effects associated with heat diffusion. From an experimental standpoint, kinematic data obtained by DIC techniques were used to estimate a stress-strain response and then compute the volume deformation energy within a hysteresis loop. Moreover, thermal images produced by an infrared camera were used to estimate the distribution of heat sources generated by the deformation. These sources may be due to dissipative and/or thermomechanical coupling effects. Several application examples were chosen to illustrate the diversity of mechanisms that induce hysteretic responses.

Keywords: full-field measurments; digital image correlation; infrared thermography; continuum thermomechanics; energy balance; dissipative and coupling effects; stored energy; hysteresis loop.

1. Introduction

The deformation of solid materials is nearly always accompanied by temperature variations. These variations are induced by heat sources of a different nature and vary in their intensity and spatial distribution. They also depend on the diffusivity of the material and the boundary conditions, which implies that the thermal information is not completely intrinsic to the material behavior. Besides, temperature variations induced in solid materials by quasi-static mechanical loadings may remain low and are still often neglected. Consequently, from a modeling standpoint, these experimental facts have implicitly prompted the marked development of isothermal mechanical models in the literature.

 doi:10.1016/j.piutam.2012.05.003

Nevertheless, the temperature variations, no matter how small they may be, may correspond to amounts of heat that cannot be neglected in the energy balance, and should consequently be taken into account in the thermomechanical modeling. Mandel and Bui were among the first to show the great benefits of combining the mechanical and energy aspects of the deformation mechanisms interpreted within a thermodynamic framework [1-2].

For this reason, over the two last decades, we developed digital image correlation (DIC) and infrared thermography (IRT) techniques in an effort to identify deformation energy and heat source distributions from surface displacement and temperature fields during a deformation process [3-5]. We showed that the nature of heat sources strongly depended on the material behavior. These sources may represent intrinsic dissipation of energy (plasticity, viscosity, damage, etc.) [6, 7], or result from thermomechanical coupling mechanisms (thermoelasticity, rubber elasticity, latent heat of solid-solid phase transition, etc.) [8, 9]. Generally speaking, energy information associated with material behavior is still seldom available in the literature. This kind of information is nevertheless of great interest in that it characterizes the irreversibility of deformation mechanisms and reveals the thermal sensitivity of the material. From a modeling standpoint, coupling sources and dissipation are respectively related to state and evolution constitutive equations, and consequently provide useful energy safeguards to check the consistency of (thermo) mechanical models.

This paper focuses on the energy signatures of materials during cyclic loading when stabilized mechanical hysteresis loops can be observed. It first briefly reviews the theoretical background used to define the energy balance during such thermodynamic processes. Then it describes the different devices involved in the experimental setup and the data processing developed for quasi-static testing. Finally, it presents selected examples of kinematic, thermal and calorimetric results: the selection is made to illustrate the diversity of mechanisms that induce hysteretic responses. At low strain, the rate dependence of the “pure” thermoelastic behavior is first recalled. Secondly, the viscothermoelasticity of PMMA and PC polymers is analysed during olygocyclic tests. Other types of strong thermomechanical couplings are evoked with the solid-solid phase transition of a mono-crystalline CuAlBe shape memory alloy and the entropic elasticity of natural rubber. Finally, the dissipated and stored energies that accompany the high cycle fatigue (HCF) of a dual phase steel are shown. Throughout the paper, the main consequences in terms of understanding and modeling the material behavior are discussed.

2. Energy balance

In the framework of the thermodynamics of irreversible processes with internal state variables, the equilibrium state of each volume material element is characterized by a set of n state variables [10]. For low deformation, the chosen state variables are the absolute temperature T, the strain tensor ε, and the n-2 scalar components (α_1, …, α_{n-2}) defining a vector α of "internal" variables, introduced to model the micro-structural state of the material. By construction, the thermodynamic potential is the specific Helmholtz free energy ψ.

2.1. Mechanical energy rates

The Cauchy stress tensor σ can then be split into two parts: the reversible part σ^r, which is the conjugated variable associated with the strain, with respect to the volume free energy $\rho\psi$ ($\sigma^r=\rho\partial\psi/\partial\varepsilon$), and the irreversible part σ^{ir}. For low strain, the deformation energy rate can then be written as:

$$w^{\bullet}_{def} = \sigma : \dot{\varepsilon} = \underbrace{\sigma : \dot{\varepsilon} - \overbrace{(\rho\psi_{,\varepsilon} : \dot{\varepsilon} + \rho\psi_{,\alpha}.\dot{\alpha})}^{w^{\bullet}_e + w^{\bullet}_s}}_{w^{\bullet}_d} + w^{\bullet}_e + w^{\bullet}_s \qquad (1)$$

where ρ denotes the mass density. According to the material and the loading path, the deformation energy rate may involve energy dissipation ($w^{\bullet}_d$), elastic ($w^{\bullet}_e$) and stored ($w^{\bullet}_s$) energy storage/release. Note that the non-standard notation $w^{\bullet}$ specifies that the energy rate is path-dependent (*i.e.* w is not necessarily a state function).

2.2. Heat sources

Combining the first and second principles of thermodynamics leads to the local heat diffusion equation:

$$\rho C\dot{T} - \mathrm{div}(k\,\mathrm{grad}T) = w^{\bullet}_d + \underbrace{\rho T\psi_{,\varepsilon T} : \dot{\varepsilon} + \rho T\psi_{,\alpha T}.\dot{\alpha}}_{w^{\bullet}_{thc}} + r_e \qquad (2)$$

where C is the specific heat, and k is the heat conduction tensor. The left-hand side consists of a differential operator applied to the temperature, while the right-hand side pools the various types of heat source: the intrinsic dissipation $w^{\bullet}_d$, the thermo-mechanical coupling sources $w^{\bullet}_{thc}$ (i.e. heat sources induced by a thermo-mechanical coupling mechanisms), and the possible external heat supply r_e (e.g. radiation exchanges). The intrinsic dissipation characterizes the material degradation accompanying the irreversible microstructure transformation, while the thermo-mechanical heat sources reflect the thermo-sensitivity of the matter, indicating that the mechanical, microstructural, and thermal states are closely coupled.

2.3. Energy balance over a load-unload cycle

Let us now consider a load-unload cycle, where $A = (T_A, \varepsilon_A, \alpha_A)$ and $B = (T_B, \varepsilon_B, \alpha_B)$ denote the thermo-mechanical states of the material at the extremities of the process. Let us then consider the energy balance corresponding to the three following situations:

- case 1: $A \neq B$, this general situation can be illustrated by the schematic stress-strain diagram proposed in Fig. 1.
- case 2: $A \neq B$ and $\varepsilon_A \doteq \varepsilon_B$, a mechanical cycle is then associated with the load-unload test. The stress-strain diagram shows a hysteresis loop.
- case 3: $A = B$, the mechanical cycle is now a thermodynamic cycle.

Following Eq.(1), the intrinsic dissipation is then the difference between the deformation energy rate and the sum of the elastic and stored energy rates. Both principles of thermodynamics give an alternative expression of the volume deformation energy associated with the load-unload test:

$$w_{\mathrm{def}} = \int_{t_A}^{t_B} w^{\bullet}_d \,\mathrm{d}t + \int_{t_A}^{t_B} (w^{\bullet}_{\mathrm{e}} + w^{\bullet}_{\mathrm{s}})\mathrm{d}t = \int_{t_A}^{t_B} w^{\bullet}_d \,\mathrm{d}t + \int_{t_A}^{t_B} (\rho\dot{e} - \rho C\dot{T})dt + \int_{t_A}^{t_B} w^{\bullet}_{\mathrm{thc}} \,\mathrm{d}t \,, \qquad (3)$$

where e is the specific internal energy.

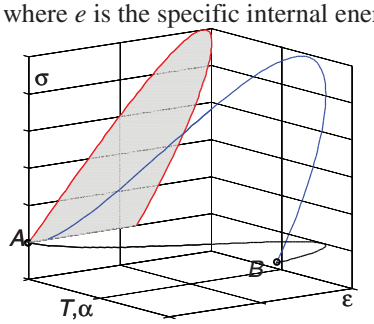

Fig. 1. Schematic stress-strain diagram for a load-unload test; t_B-t_A is the cycle duration

Equation (3) shows that:
- case 1: in the general case, the balance of deformation energy during a load unload test involves energy dissipation, internal energy variations, variation of heat stored in the material, coupling heat sources.
- case 2: the deformation energy then corresponds to the "generalized area" A_h of the different hysteresis loops in the planes σ_{ij}-ε_{ij}, $i, j = 1,2,3$.
- case 3: for a thermodynamic cycle, these hysteresis loops are only due to dissipation and couplings since the heat capacity ρC is assumed to be constant.

The energy balance form then gives the restricted conditions for which the dissipated energy can be estimated by computing the hysteresis area of a uniaxial load-unload cycle. This underlines the necessity of analysing the thermal effects to verify if a mechanical cycle is also a thermodynamic cycle, and of checking the relative importance of coupling effects.

3. Combining DIC-IRT data

3.1. Experimental set-up

The experimental set-up designed to derive local energy balances has been regularly improved over the last ten years [3-5, 7]. It currently involves an MTS hydraulic testing machine (frame: 100 kN, load cell: 25 kN), a Camelia 8M high resolution CCD camera and a CEDIP Titanium infrared camera (Fig.2). The optical axis of both cameras was set perpendicularly to the frame of the testing machine, and remained fixed during the test. The visible and infrared optical lenses were chosen to ensure a similar space resolution of about 0.1 mm. Visible and infrared images were simultaneously recorded on each side of the sample surface, and thin samples were therefore used. Each camera was controlled by a separate computer although a specific electronic device was designed to synchronize the frame grabbing of the two cameras. Using this device, the synchronization error between the two cameras was estimated to be less than 50 μs. Reference speckle and infrared images were mapped by determining the affine transformation coefficients (rigid body movement and homothetic transformation) of the shape of a calibrated target. The accuracy of this map-to-map correspondence was estimated at about 0.5 pixel (i.e. 50 μm), satisfactory for a mesocopic behavioral analysis. For each acquisition time, the thermal data given by the IR camera (measured in the current Eulerian configuration) were linearly interpolated spatiotemporally using the positions of the deformed configuration given by the DIC computation. This operation allowed the material surface element (MSE) associated with the DIC mesh to be tracked so that the extent of the volume heat rate induced by matter convection and associated with the particular time derivative of the temperature could subsequently be computed and checked. Readers interested in the many tricky metrology issues and in a detailed presentation of the image processing can refer to [7].

The sample surface in front of the CCD camera was conventionally speckled with white paint on a black background to optimize the contrast of the local optical signature, while the surface emissivity of the sample gauge part placed in front of the IR camera was increased and homogenized using flat black paint.

Fig. 2. Experimental set-up: (front): CCD camera and cold light sources, (back): IRFPA camera. The grips and columns of the testing machine are roughly wrapped to avoid parasitic reflection interference.

3.2. Mechanical data processing

Mechanical image processing aims to derive plane stress patterns from the strain field within the sample gauge part during uniaxial loading [7]. The stress field estimate is naturally required to compute the deformation energy. This computation is performed under the following assumptions. Although some are obviously relevant, others may be more questionable (particularly when strain localization or damage develops). These main assumptions are: (*i*) the stress triaxiality is neglected and the plane stress hypothesis is adopted, (*ii*) the transformation remains isochoric (when damage develops, a transversal isotropy hypothesis may be chosen instead), (*iii*) the overall loading is purely uniaxial (no shear loading) and the tensile stress is uniformly distributed over each cross-section, (*iv*) the lateral boundary of the specimen gauge part is stress free.
Under such hypotheses, fields of tensile, shear and transverse stress components (for thin flat samples) or radial stress components (for cylindrical samples) were computed, with these components being deduced via integration of the equilibrium equations.

3.3. IR image processing

The goal of IR image processing is at least twofold: first, to obtain reliable surface temperature fields and second, to derive the corresponding distribution of heat sources from these thermal data. A pixel calibration of the IRPFA camera was proposed in [11] which allowed a thermal resolution of about 20 mK, in the laboratory conditions. Special efforts were focused on reducing parasitic radiations (see Fig.2) and keeping the room temperature as constant as possible.
An averaged version of the heat diffusion equation is proposed to compute the heat source distribution from surface temperature fields. The averaging operation was performed over the specimen thickness. We showed [5] that the surface temperature assessed by the IR camera, remained close to the mean depth-

wise averaged temperature, even for penalizing heterogeneous heat source distributions and because of the relatively good heat diffusivity of solid materials.
Additional hypotheses were put forward to pass from temperature to heat sources. The following strong hypotheses have been put forward so far:
- ρ and C are material constants, independent of the thermodynamic state.
- k remains constant and isotropic during the test (i.e. $k_{ij} = k\,\delta_{ij}$).
- the external heat supply r_e due to heat exchange by radiation is time-independent, so the equilibrium temperature field T_0 verifies $-\Delta T_0 = r_e$. It is then convenient to consider the temperature variation θ defined by $\theta = T - T_0$.
Finally, taking the linearity of the heat diffusion equation and that of the thermal boundary conditions (linear heat losses) into account, approximation functions were proposed to perform a local spatiotemporal fit of the thermal data and estimate the differential operators present in the heat equation and then the heat sources. Kinematic data obtained by DIC were used to compute, if necessary, the convective terms due to the material time derivative of the temperature [7].

4. Application examples

Several examples of behavior were chosen to show the diversity of the energy signature of mechanical hysteresis loops. At this level, it should be mentioned that a still widespread reaction is to associate – more or less implicitly – the hysteresis area with the dissipative effects due to microstructural material degradation. As shown above by the thermodynamic analysis (Eq.(3)), energy storage and/or coupling effects may also generate mechanical hysteresis loops, and it is essential to estimate the relative importance of these mechanisms, as the consequences in terms of behavior modeling are particularly critical.

4.1. Hysteresis induced by coupling mechanisms

When a stabilized mechanical cycle is also a thermodynamic cycle, the hysteresis area only has two possible origins: microstructural energy dissipation and coupling mechanisms. The academic case of linearized thermoelasticity can be evoked as evidence of this second possibility. Here, the only allowed source of irreversibility is then due to the heat diffusion. For simplicity, a "0D description" can be considered. Indeed, 3D heat diffusion mechanisms can be bypassed assuming linear heat losses depending only on the temperature variation [4]. In such a simplified context, the main equations of the thermoelastic problem are then summed up by the following coupled algebraic and differential equations:

$$\begin{cases} \sigma = E(\varepsilon - \lambda_{th}\theta) & (a) \\ \dot{\theta} + \dfrac{\theta}{\tau_{th}} = -\dfrac{\lambda_{th} E(T_0 + \theta)\,\dot{\varepsilon}}{\rho C} & (b) \end{cases}, \qquad (4)$$

where σ is the tensile stress, ε the longitudinal strain, τ_{th} a time constant characterizing the heat losses, E the Young's modulus and λ_{th} the linear thermo-dilatation coefficient. During a cyclic strain-controlled test $\varepsilon = \varepsilon_0 \sin(2\pi f_L t)$, where ε_0 is the stress amplitude and f_L the loading frequency, one experimentally observes, after some cycles, that the temperature variations progressively become periodic and symmetric with respect to the time axis. Once the periodic regime is reached, the mechanical cycles become thermodynamic cycles and the hysteresis area A_h, according to Eq. (5), reads:

$$w_{def} = A_h = \int_t^{t+f_L^{-1}} w_{the}^{\bullet} \mathrm{d}\tau = w_{the}\,. \qquad (5)$$

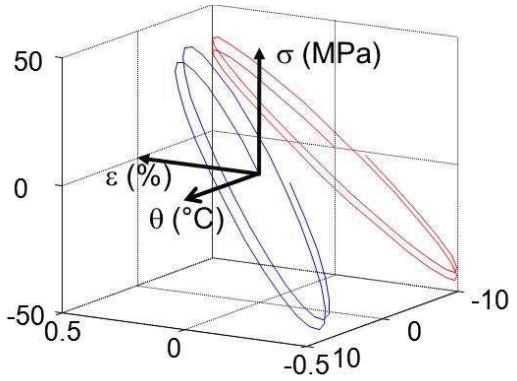

Fig. 3 Thermoelastic cyclic responses; the typical values chosen for the simulation are close to polymer characteristics: E= 1000 MPa, ρ=1000 kg.m^{-3}, C=1000 J.kg^{-1}.°C^{-1}, τ_{th} = 20 s. The dilatation coefficient was multiplied by 100 (λ_{th}=5.10^{-3} °C^{-1}) to amplify the hysteresis effect induced by coupling and heat diffusion. Loading parameters were, f_L=0.05 Hz, ε_0=0.005.

4.2. Visco- vs. thermo-elasticity

In non-adiabatic and non-isothermal situations, thermoelastic coupling then induces rate dependence. It may be interesting to highlight this rate dependence by writing a rheological equation. From equations Eq.(4a-4b), we get, by substituting the temperature, in case of small thermal variations ($\theta << T_0$):

$$\sigma + \tau_{th}\dot{\sigma} \approx E\varepsilon + E\tau_{th}\left(1+\frac{E\lambda_{th}^2 T_0}{\rho C}\right)\dot{\varepsilon}\ . \qquad (6)$$

This rheological equation looks like those obtained in linear viscoelasticity. This similarity naturally complicates the behavior analysis, particularly if the thermoelastic effects are, from a calorimetric standpoint, greater than the viscous effects. For such materials, the results, given by standard visco-analysis and leading to the determination of complex moduli, are harder to interpret because of the superimposition of two similar independent time effects respectively induced by viscous dissipation and thermoelastic coupling.

For example, PMMA and PC polymers, very often used in industrial applications, were already considered in [11, 12]. The temperature corresponding to the first sub-vitreous relaxation peak of the PMMA was slightly greater than the room temperature at which the tests were performed ($T_0 \approx$ 20-24°C), while the relaxation peak temperature of the PC polymer was highly negative. Consequently, at around room temperature, the PC samples showed greater molecular mobility than the PMMA samples. Due to this property, the PC samples showed good ductility while the PMMA samples remained particularly brittle. As the glass transition temperature of both polymers is greater than 100°C, they naturally remained in a glassy state during the deformation tests. The main thermo-mechanical characteristics of both materials were grouped in Table 1. Standard dog bone shaped test specimens were used with the following gauge part sizes: length (60 mm), width (10 mm), and thickness (4 mm).

Figures 4a and 5a show the stabilized stress-strain hysteresis loop for both materials during tests at a constant absolute strain rate value (about 10^{-4} s^{-1}) with a constant stress range. The primacy of the thermoelastic effects over the dissipation can then easily be suspected due to the temperature variation. We observed a distinct cooling of the specimen during the loading stages and heating during the unloading stages, with the mean temperature over each load-unload cycle being approximately zero.

Table 1. Main thermophysical properties of PMMA and PC

	origin	PMMA	PC
ρ (Kg.m$^{-3)}$	measured	1160	1190
C (J.Kg^{-1}.°C^{-1})	Atofina	1450	1200
κ (W.m^{-1}.K$^{-1)}$	Atofina	0.17	0.2
$\lambda_{th} \times 10^6$(°C^{-1})	measured	7	7
E (MPa)	measured	3650	2650

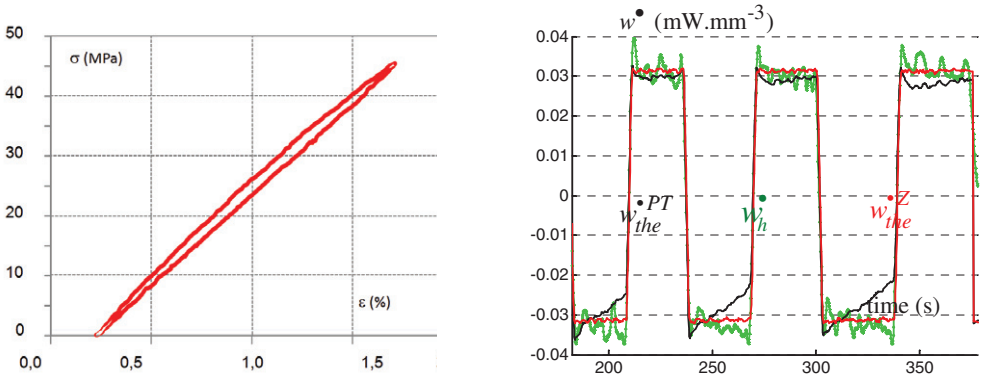

Fig. 4. (a) example of stabilized stress-strain response (PMMA); primacy of thermoelastic effects: $w_h^{\bullet\Theta}$, $w_{the}^{\bullet Z}$, $w_{the}^{\bullet PT}$ patterns associated with load-unload cycles with increasing stress ranges and a constant absolute strain rate value ($|d\varepsilon/dt|$=4.35 10^{-4} s^{-1}).

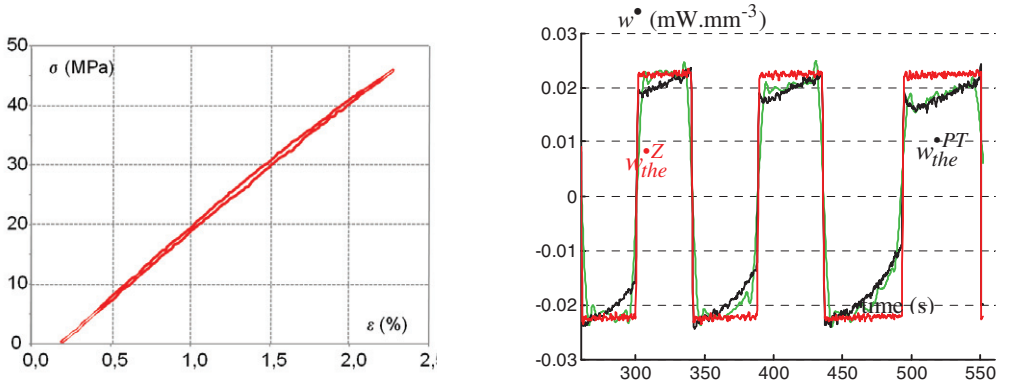

Fig.5. (a) example of stabilized stress-strain response (PC); (b) primacy of thermoelastic effects: $w_h^{\bullet\Theta}$, $w_{the}^{\bullet Z}$, $w_{the}^{\bullet PT}$ patterns associated with load-unload cycles with increasing stress ranges and a constant absolute strain rate value ($|d\varepsilon/dt|$=4.35 10^{-4} s^{-1}).

Figures 4b and 5b show the time variation of the overall heat sources $w_h^{\bullet\Theta}$ derived from the IR thermal data during cycles performed at a constant (absolute) strain rate with an increasing stress range. They confirmed the negligible character of the dissipation. We also plotted the numerical predictions of thermelastic sources given by Zener and Poynting-Thomson type models where the elastic branches were

replaced by thermoelastic ones [12]. We then noticed that the series and parallel viscoelastic models were no longer equivalent when thermoelastic effects were taken into account.

Regarding the PMMA behavior, Fig. 4b shows that variations in $w_h^{\bullet\Theta}$ and $w_{the}^{\bullet Z}$ remained close at all stress levels. Conversely, the source $w_{the}^{\bullet PT}$ was quasi linear throughout the loading, while $w_h^{\bullet\Theta}$ remained almost constant. Regarding the PC behaviour, estimates of the same sources were plotted in Fig. 5b. A better prediction was obtained with the PT type model.

For these two studied materials, it should be noted that the order of magnitude of the thermoelastic source amplitude was about 60 μW.mm^{-3}, for a dissipation intensity of less than 2 μW.mm^{-3}, i.e. order of magnitude of heat sources corresponding to the thermal noise.

4.3. Extension to other couplings

Naturally the influence of the material thermo-sensitivity on the cyclic stress-strain response is not limited to the linear thermo-dilatability. Other types of strong thermo-mechanical couplings exist.

We first mention the solid-solid phase change (change of crystallographic network) when it is accompanied by latent heat (first order phase transition). More particularly in Fig.6, we considered the austenite-martensite phase transition of monocrystalline CuAlBe during a stress-controlled cyclic test at room temperature.

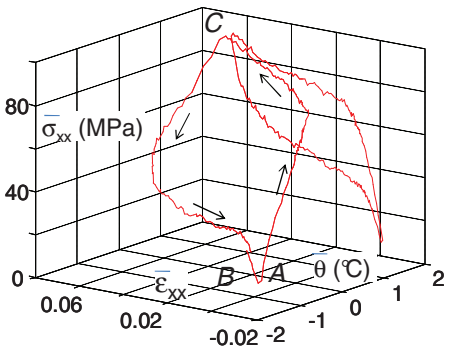

$\left[\bar{w}_{def}\right]_A^C$	4.9 mJ.mm^{-3}
$\left[\bar{w}_h\right]_A^C$	28 mJ.mm^{-3}
$\bar{A}_h = \int_{t_A}^{t_B} \bar{w}_{def}^{\bullet}\,\mathrm{d}t$	1.9 mJ.mm^{-3}
$\bar{R}_M = \dfrac{\bar{A}_h}{\int_{t_A}^{t_C} \bar{w}_{def}^{\bullet}\,\mathrm{d}t}$	0.39
$\bar{R}_T = \dfrac{\int_{t_A}^{t_B} \bar{w}_h^{\bullet}\,\mathrm{d}t}{\int_{t_A}^{t_B} \lvert\bar{w}_h^{\bullet}\rvert\,\mathrm{d}t}$	0.026

Fig.6. (a) Mean* cyclic thermomechanical response of CuAlBe SMA; (b) mean* energy balance ("mean*" symbolizes the average over the specimen gage part and is here symbolized by (¯)).

Fig. 6a shows the mean thermodynamic path of the specimen gage part during a load-unload cycle. We claim that the stress induced phase change at room temperature (294 K) must be considered as an anisothermal process since temperature variations are associated with heat quantities more than fivefold greater than the mechanical energy spent in the specimen deformation. Temperature variations, induced by the latent heat of phase change, influence the kinetics of the stress-induced phase transition. In our opinion, this clearly warrants its interpretation as a strong thermomechanical coupling mechanism. The conventional hysteresis loop of shape memory alloys (SMAs) was also plotted in Fig. 6a, projecting the thermodynamic path onto the stress-strain plane. Fig. 6b indicates the deformation energy spent during loading, the heat evolved during this loading sequence and the energy corresponded to the hysteresis area. It also proposes two indicators: R_M reflects the mechanical importance of hysteresis, while R_T determines the relative importance of the dissipative and coupling effects, over the cycle, i.e. 1 for a purely

dissipative cycle and 0 for a purely reversible cycle. When there is only low irreversibility induced by heat diffusion, R_T also remains low [9, 13, 14].

The second example of thermomechanical coupling corresponds to the so-called entropic elasticity of rubber-like materials [15]. Here the microstructural mechanism is a recoverable stress-induced reorientation of the macromolecular chains. The molecular mobility of such materials led several authors [16, 17] to compare rubber materials with a perfect gas, assuming that the internal energy of such materials is only temperature dependent. The literature also shows that the entropic elasticity prevails at high strain while, for low strain, there is a competition between standard and entropic elasticity, giving rise to the thermoelastic inversion first observed by Antony et al. [18]. Hereafter, the chosen strain range allowed us to just consider the entropic elasticity. Fig.7a shows the mean thermodynamic path and the load-elongation curve projected onto the mechanical plane (λ is the longitudinal extension ratio). It is interesting to note that the mean temperature over a short cycle is decreasing during the first five cycles. For longer series of short cycles, we observed that the temperature variations progressively became periodic and symmetric. The transient effect observed here is due to heat exchanges with the surrounding environments. Fig. 7b presents the time evolution of the deformation energy rate and of the heat rate induced by strain. To compare the different energy mechanisms, the volume energy rate was divided by the volume heat capacity ρC of the material. This gave the volume energy rate expressed in $K.s^{-1}$ instead of $MW.m^{-3}$. Despite the noise on heat sources due to thermal fluctuations, both energy rates are close which is in line with the perfect gas analogy.

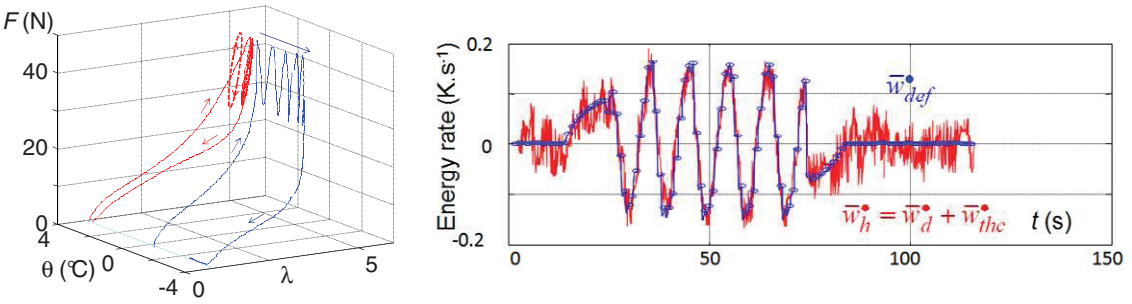

Fig.7. (a) Cyclic thermomechanical response of natural rubber specimen; (b) mean energy rates.

As for pseudoelastic SMAs, intrinsic dissipation was hardly detectable for this loading frequency. Tests at loading frequencies of about 20-30 Hz are currently under way to amplify the dissipative effects.

4.4. Energy storage

The examples presented below highlight that various thermomechanical couplings played a great role in the understanding of the mechanical cyclic response. The last example deals with the high cycle fatigue (HCF) of steel. The example focuses on a dual phase steel (DP 600) which is a high strength steel with a ferrite and martensite microstructure. It is widely used because its HCF limits are greater than the conventional tensile yield stress.

For elastoplastic materials, cyclically loaded within the so-called macroscopic elastic domain, it can be shown that the thermoelastic energy over a complete number of cycles remain negligible [6] when the thermoelastic properties can be assumed to be constant over this period. The small hysteresis area shown in Fig.8a then involves dissipated and possibly stored energies. Both represent the energy signature of the microstructure evolution (typical development of persistent slip bands). The stored energy gives

information required to estimate this change of microstructural state, while the dissipation quantifies the irreversible character of this change.

Fig.8b shows the pattern of the deformation and dissipated energy rates computed over the specimen gauge part. Tests involved loading blocks, with each block being performed at constant $\Delta\sigma$ with R_σ=-1 and f_L = 30 Hz. Tests were constructed in stages, with each stage including a series of 5 "mini" blocks of 3 000 cycles per block with increasing $\Delta\sigma$ varying regularly from 175 up to 580 MPa, and a large block of 100 000 cycles performed at $\Delta\sigma$ = 580 MPa.

The stages were repeated until a macro-crack occurred. Results corresponding to the two first series of mini blocks were plotted in Fig.8b. They allowed us to construct the curve $\overline{w}_d^{\bullet}$ vs. $\Delta\sigma$ at a "constant" fatigue state. Between these two series of mini blocks, a large block was performed, close to the fatigue limit so as to speed up the fatigue progress. For large blocks, camera shots were regularly taken to check the monotonic evolution of dissipative effects. We observed that the dissipated energy was approximately half of the deformation energy which means that the dissipated and stored energy were of the same order of magnitude. This drift in the energy response induced by the fatigue progress is here symbolized in Fig.8b by vertical arrows. We noted that the drift in the dissipation curve for high stress range is more important that the drift of the deformation energy rate. In other words, the capability of the material to store energy and adapt its microstructure decreases cycle by cycle, reflecting a low but regular material degradation. This drift will be used as an energy indicator to model and identify the kinetics of the fatigue progress.

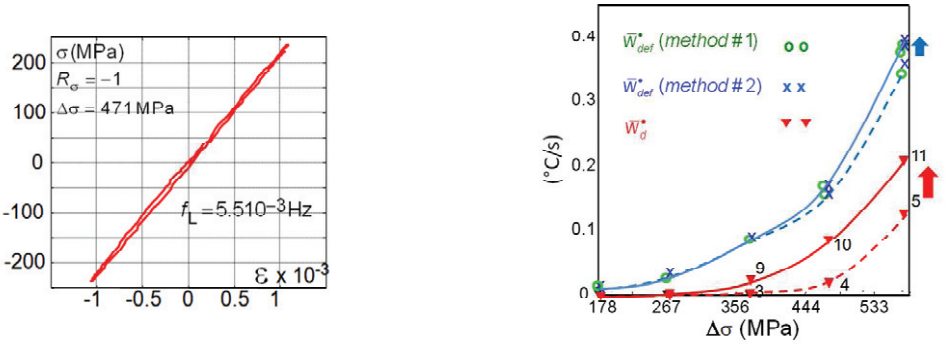

Fig.8. (a) Mean** stress-strain response of a DP600 specimen (R_σ is the stress ratio, $\Delta\sigma$ the stress range and f_L the loading frequency), (b) mean** energy rates per cycle; a description of the two methods can be found in [19], "mean**" here stands for the averaged value over the specimen gage part and over the block of cycles.

5. Concluding comments

When focusing on the cyclic loading, the aim of this paper was to showcase the diverse range of experimental information which is now provided by quantitative imaging techniques to characterize and identify the behavior of materials. The combined use of DIC and IRT enabled us to derive the local energy balance. In particular, the determination of the heat source which accompanies the cyclic deformation process is critical. Thermodynamic analysis of the energy balance showed that the influence of dissipated energy on the cyclic response was not systematically predominant. Thermomechanical coupling mechanisms or energy storage (internal energy variations) may have a significant influence on the hysteretic stress-strain response. Several illustrative examples showed that these energy signatures gave precious information on the nature and evolution of cyclic deformation mechanisms.

References

[1] Mandel J, Energie élastique et travail dissipé dans les modèles, *Cahiers du Groupe Français de Rhéologie*, 1965, **1**, 1,9-14.
[2] Bui HD, Dissipation d'énergie dans une déformation plastique, *Cahiers du Groupe Français de Rhéologie*, 1965, **1**, 1,15-19.
[3] Wattrisse B, Chrysochoos A, Muracciole JM and Nemoz-Gaillard M, Analysis of strain localization during tensile test by digital image correlation, *J. Exp. Mech.*, 2000, **41**, 1, 29-38.
[4] Chrysochoos A and Louche H, An infrared image processing to analyze the calorific effects accompanying strain localisation, *Int. J. of Engng. Sci.*, 2000, **38**, 1759-1788.
[5] Berthel B, Chrysochoos A, Wattrisse B and Galtier A, Infrared image processing for the calorimetric analysis of fatigue phenomena, *Exp. Mech.*, 2008, **48**, 79-90.
[6] Boulanger T, Chrysochoos A, Mabru C and Galtier A, Dissipative and thermoelastic effects associated with the fatigue behavior of steels, *Int. J. of Fatigue*, 2004, **26**, 221-229.
[7] Chrysochoos A, Wattrisse B, Muracciole JM, El Kaim Y, Fields of stored energy associated with localized necking of steel, 2009, *J. Mech. Mat. Str.*, **4**, 2, 245-262.
[8] Wattrisse B, Muracciole JM and Chrysochoos A, Thermomechanical effects accompanying the localized necking of semi-crystalline polymers, *Int. J. of. Therm. Sci.*, 2001, **41**, 422-427.
[9] Peyroux R, Chrysochoos A, Licht C and Löbel M, Thermomechanical couplings and pseudoelasticity of shape memory alloys, *Int. J. Engng Sci.*, 1998, **36**, 4, 489-509.
[10] Germain P, Nguyen QS and Suquet P, Continuum Thermomechanics, *J. Appl. Mech.*, 1983, **50**, 4B, 1010-1020.
[11] Honorat V, Moreau S, Muracciole J.M, Wattrisse B and Chrysochoos A, Calorimetric analysis of polymer behaviour using a pixel calibration of an IRFPA camera, *Int J. on Quantitative Infrared Thermography*, 2005, **2**, 2, 153-172.
[12] Moreau S, Chrysochoos A, Muracciole JM and Wattrisse B, Analysis of thermoelastic effects accompanying the deformation of PMMA and PC polymers, *C. R. Acad Sci. II, 2005*, **333**, 8, 648-653.
[13] Chrysochoos A, Pham H, Maisonneuve O, An experimental analysis of the thermomechanical behavior of a CuZnAl shape-memory alloy, *C.R. Acad. Sci. II*, 1993, **316**, 8, 1031-1036.
[14] Chrysochoos A, Lobel M, Maisonneuve O, Thermomechanical coupling of pseudoelastic behavior of CuZnAl and NiTi alloys, *C.R. Acad. Sci. II*, 1995, **320**, 5, 217-223.
[15] Ferry JD, Viscoelastic properties of polymers., J Wiley & Sons, 1980.
[16] Chadwick P, Creasy CFM, Modified entropic elasticity of rubberlike materials, *J. Mech. Phys. Sol.*, 1984, **32**, 337-357.
[17] Ogden RW, On the thermoelastic modeling of rubber-like solids, *J. of Thermal Stresses*, 1992, **1**, 4, 553-557.
[18] Anthony RL, Caston RH, Guth E, Equations of state for naturals and synthetic rubber like materials: unaccelerated natural soft rubber, *J. phys. Chem.*, 1942, **46**, 826-840.
[19] Chrysochoos A, Berthel B, Latourte F, Galtier A, Pagano S, Wattrisse B, Local energy analysis of high-cycle fatigue using digital image correlation and infrared thermography, *J. of Strain Anal. for Engng Design*, 2008, **43**, 6, 411-421.